Hot-carrier convection in graphene Schottky junctions

Joaquin F. Rodriguez-Nieva[1], Mildred S. Dresselhaus[1,2], and Justin C. W. Song[3*]
[1] *Department of Physics, Massachusetts Institute of Technology, Cambridge, MA 02139 USA*
[2] *Department of Electrical Engineering and Computer Science, Massachusetts Institute of Technology, Cambridge, MA 02139, USA and*
[3] *Walter Burke Institute for Theoretical Physics and Institute of Quantum Information and Matter, California Institute of Technology, Pasadena, CA 91125 USA*

The exposed nature of the 2D electronic states in van der Waals materials are expected to render vertical transport in heterostructures highly susceptible to interfaces. We show that a new channel for energy transport - hot carrier convection - can be engineered in graphene Schottky junctions/interfaces. In this channel, hot carriers are vertically extracted through thermionic emission of graphene hot carriers into a semiconductor, thereby cooling the graphene electronic system. Large hot carrier convective energy currents can overwhelm conventional diffusive electronic energy transport, as well as dominate over electron-lattice cooling. Crucially, hot carrier convection features strongly coupled energy and charge currents that run vertically out of the graphene plane. This yields clear experimental signatures such as large and tunable responsivities of graphene Schottky junction photodetectors with a non-monotonic temperature dependence, opening up new approaches for engineering energy transport in 2D heterostructures.

Vertical heterostructures comprising layers of van der Waals (vdW) materials have recently emerged as a platform for designer electronic interfaces [1]. Of special interest are heterostructures which feature tunable interlayer charge transport characteristics, exemplified by G/X Schottky junctions [2–10]; here G denotes graphene, and X is a semiconductor material, such as Si, MoS_2, WSe_2. These junctions are characterized by Schottky barrier heights ϕ that span two orders of magnitude $\phi \approx 0.01 - 1\,\mathrm{eV}$[2–5] and exhibit *in-situ* control. The relatively small ϕ achievable across the G/X interface, combined with slow electron-lattice cooling mechanisms in graphene that enable long-lived hot carriers (elevated electronic temperatures, T_g, different from that of the lattice, T_0) [11–16], make graphene Schottky junctions a prime target for studying novel vertical energy transport regimes.

Here we show that a new channel for hot carrier cooling can arise across graphene Schottky junctions: hot-carrier *convection*. As shown schematically in Fig. 1a, convective hot carrier cooling proceeds via the thermionic emission of graphene hot carriers with energy larger than the Schottky barrier into the semiconductor; at steady state, the same number of cold carriers are injected at the Fermi surface through an ohmic contact yielding a net flow of heat $\mathcal{J}_\mathbf{q}^\perp$ out of the graphene electronic system. We find that $\mathcal{J}_\mathbf{q}^\perp$ can be significant (see Fig. 1c) when $k_\mathrm{B}T_\mathrm{g} \sim \phi$, dominating over acoustic-phonon cooling [11, 12] in pristine graphene Schottky junctions; $\mathcal{J}_\mathbf{q}^\perp$ is competitive with disorder-assisted cooling [13–15] in more dirty devices.

As we argue below, $\mathcal{J}_\mathbf{q}^\perp$ in graphene Schottky junctions also outcompete conventional modes of diffusive electron energy transport, namely, in-plane (lateral) and out-of-plane (vertical) electronic thermal conduction. As a result, clean G/X Schottky interfaces (where electron-lattice cooling is small) grant access to the regime of convective electronic heat transport. This regime is reminiscent of convection in liquids and gases, but is atypical for thermal transport in solids [17].

Importantly, carriers emitted thermionically also carry charge. As a result, convective heat transport is characterized by a vertical energy current, $\mathcal{J}_\mathbf{q}^\perp$, that is locked to vertical charge current, $\mathcal{J}_e^\perp$. Indeed, an energy ϕ is transported per carrier extracted across the G/X junction (Fig. 1a) yielding a strong charge-energy coupling $\mathcal{L}$ given by

$$\mathcal{J}_e^\perp = \mathcal{L}\mathcal{J}_\mathbf{q}^\perp, \quad \mathcal{L} = \frac{e}{\phi} \times \alpha(\tilde{T}_\mathrm{g}, \tilde{T}_0). \tag{1}$$

Here e is the electron charge, $\tilde{T}_0 = k_\mathrm{B}T_0/\phi$ is the dimensionless ambient temperature (temperature of the lattice and semiconductor), $\tilde{T}_\mathrm{g} = k_\mathrm{B}T_\mathrm{g}/\phi$ is the dimensionless hot carrier temperature in graphene, and α is a dimensionless function (see text below) plotted in Fig. 1b. The function α can take values close to unity, allowing $\mathcal{L}$ to be on the order of $e/\phi = 10\,\mathrm{A/W}$, for $\phi = 100\,\mathrm{meV}$.

Strong charge-energy current coupling [Eq. (1)] is very appealing for achieving enhanced performance in graphene-based optoelectronics. This is because fast intraband Auger-type scattering [18, 19] allows absorbed photon energy flux in graphene, $\mathcal{J}_\mathbf{q}^\mathrm{in}$, to be efficiently captured as heat by ambient carriers in graphene; this process produces hot carriers [18, 19]. Strong $\mathcal{L}$ in G/X Schottky junctions provides a novel strategy for harvesting these photoexcited hot carriers to produce electrical signals. An important figure of merit is the conversion between incoming photon energy flux, and detected photocurrent, encoded in the responsivity $\mathcal{R} = \mathcal{J}_e^\perp/\mathcal{J}_\mathbf{q}^\mathrm{in}$. Indeed, in the regime where the cooling of hot carriers occurs convectively (out-of-plane), *i.e.* $\mathcal{J}_\mathbf{q}^\perp = \mathcal{J}_\mathbf{q}^\mathrm{in}$, we find $\mathcal{R} = \mathcal{L}$ values that are sizable [Eq.(1)].

As a result, $\mathcal{R}$ can be used as a diagnostic of hot carrier convection. This is most readily demonstrated

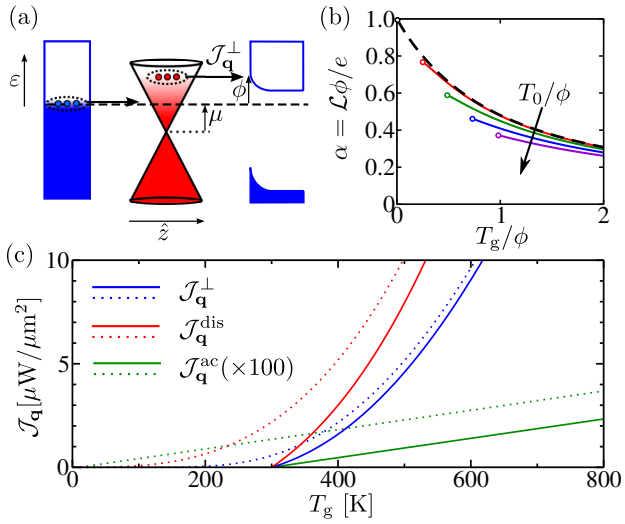

FIG. 1. (a) Schematic of convective cooling in a graphene Schottky junction: hot carriers with energies ε close to the Schottky barrier height ϕ are thermionically ejected into a semiconductor material in the out-of-plane direction $\hat{z}$, while cold carriers are injected through an Ohmic contact at the Fermi level, μ, generating a net vertical heat current $\mathcal{J}_{\mathbf{q}}^{\perp}$. (b) Normalized charge-energy coupling $\alpha = \mathcal{L}\phi/e$ as a function of normalized graphene electronic temperature, $k_B T_g/\phi$, with e the electron charge. Curves are obtained for normalized ambient temperature $k_B T_0/\phi = 0, 0.25, 0.5, 0.75, 1.0$, indicated with different colors for increasing T_0 [see Eq.(1)]; characteristic $\mathcal{L} \approx e/\phi \sim 10\,\mathrm{A/W}$ can be large (for $\phi = 100\,\mathrm{meV}$, see text). (c) convective cooling channel, $\mathcal{J}_{\mathbf{q}}^{\perp}$, compared with acoustic phonon cooling (clean case), $\mathcal{J}_{\mathbf{q}}^{\rm ac}$, and disorder-assisted cooling, $\mathcal{J}_{\mathbf{q}}^{\rm dis}$ [see text and Eq.(6)]. Shown for ambient temperature $T_0 = 300\,\mathrm{K}$ (solid lines), and $T_0 = 0$ (dotted lines). Note $\mathcal{J}_{\mathbf{q}}^{\perp}$ overwhelms $\mathcal{J}_{\mathbf{q}}^{\rm ac}$ (clean case) and is competitive with $\mathcal{J}_{\mathbf{q}}^{\rm dis}$ (dirty case). Parameter values used: $\mu = \phi = 100\,\mathrm{meV}$, $k_F \ell = 50$, and $G_0 = 10\,\mathrm{mS}/\mu\mathrm{m}^2$, see Eqs. (4) and (6).

in G/X photodetectors (Fig. 2a) wherein incident photons with energies $\hbar\omega$ *below* the energy gap Δ_X of X heat up the graphene electrons to generate hot carriers with temperature T_g, larger than the ambient temperature T_0 [14, 16, 18]. Including losses to the lattice via disorder-assisted cooling, we find that $\mathcal{R}$ is non-monotonic, peaking at an optimal operating hot carrier temperature $T_g \approx \phi/2k_B$ (Fig. 2b). Since T_g can be controlled by the incident light power and ϕ via gate voltage, non-monotonic $\mathcal{R}$ as a function of $\tilde{T}_g$ provides an easily accessible experimental signature of the strongly coupled charge and energy transport that is engineered across the G/X interface. Further, since incident $\hbar\omega$ (e.g. in the visible) can be many multiples of ϕ, we anticipate that G/X Schottky photodetectors can provide significant gains in responsivity compared to those in conventional (photovoltaic-based) photodetectors, which are limited by $\mathcal{R}^{\rm PV} \leq e/\hbar\omega$ [20], .

Other Schottky junctions (e.g. Au/Si, Ag/Si) may also display vertical energy currents. However, their large Schottky barriers ($\phi \approx 1\,\mathrm{eV}$) and fast electron-lattice cooling in the metal render the temperatures required to achieve convective transport impractical. In contrast, small ϕ and weak electron-lattice cooling in G/X allow convective cooling to be accessed in the range of technologically achievable temperatures.

We begin by modeling vertical particle transport across the G/X device, as depicted in Fig. 1a. Using the standard approach for modeling vertical graphene tunneling devices [21], wherein energy is conserved but in-plane momentum is not, we write the electron and heat current across the G/X Schottky junction as

$$\begin{bmatrix} \mathcal{J}_e^{\perp} \\ \mathcal{J}_{\mathbf{q}}^{\perp} \end{bmatrix} = \int_{-\infty}^{\infty} d\varepsilon \begin{bmatrix} e \\ \varepsilon \end{bmatrix} G(\varepsilon) \left[f\left(\frac{\varepsilon}{k_B T_g}\right) - f\left(\frac{\varepsilon}{k_B T_0}\right) \right],$$
$$G(\varepsilon) = \frac{2\pi e^2}{\hbar} D_g(\varepsilon) D_c(\varepsilon) |\mathrm{T}(\varepsilon, \phi)|^2. \qquad (2)$$

Here $G(\varepsilon)$ is a parameter with units of electrical conductance which characterizes the Schottky interface (see discussion below), D_g (D_c) is the density of states of graphene (the conduction band of the semiconductor), f is the Fermi distribution function, $f(x) = 1/(e^x + 1)$, T is the energy-dependent tunneling transition matrix element between graphene and semiconductor electronic states, and energies ε are referenced from the Fermi energy μ (see Fig. 1a). We neglect hole transport between graphene and the valence band of X assuming that the barrier height for hole transport is much larger than the corresponding one for electron transport. The function $\mathrm{T}(\varepsilon, \phi)$ contains all the microscopic information about the relevant mechanisms that couple graphene with X, such as phonons or hot-spots formed by defects. When light heats graphene electrons so that $T_g > T_0$, then Eq.(2) describes the short-circuit charge current (photocurrent) and the energy current flow, shown schematically in Fig. 1c.

At steady state, T_g is determined by energy balance of the incident absorbed power in graphene, $\mathcal{J}_{\mathbf{q}}^{\rm in}$, and the energy being dissipated by the graphene electronic system, $\mathcal{J}_{\mathbf{q}}^{\rm out}$, that includes both the convective channel, $\mathcal{J}_{\mathbf{q}}^{\perp}$, and other dissipative channels, $\mathcal{J}_{\mathbf{q}}^{\rm loss}$, (e.g. electron-lattice cooling, and diffusive heat transport discussed below). Explicitly, we have

$$\mathcal{J}_{\mathbf{q}}^{\rm in} = \mathcal{J}_{\mathbf{q}}^{\rm out} = \mathcal{J}_{\mathbf{q}}^{\perp}(T_g, T_0) + \mathcal{J}_{\mathbf{q}}^{\rm loss}(T_g, T_0), \qquad (3)$$

where we have fixed T_0 to the temperature of the ambient environment. This results from the large heat capacity and fast electron-lattice cooling in highly doped semiconductors such as Si [22]. In what follows, we shall analyze the energy/charge characteristics of G/X Schottky junctions as a function of T_g and T_0; naturally the T_g values displayed can be attained via a suitably chosen $\mathcal{J}_{\mathbf{q}}^{\rm in}$.

The depletion width, for example in G/Si interfaces [10], can be many times larger than the electron wavelength. As a result, only electrons with energies above the

effective barrier ϕ formed at the G/X interface contribute to the current; in this way, the photocurrent is thermally activated. Here we adopt a phenomenological approach to capture the essential physics independent of the microscopic details of the device. To this end, we approximate $G(\varepsilon) = G_0\Theta(\varepsilon-\phi)$ in Eq.(2), with Θ the step-function, in order to aggregate the microscopics of the junction into a single variable that can be easily measured in experiment. We emphasize that this approximation does not affect the qualitative behavior of $\mathcal{J}_e^{\perp}$, $\mathcal{J}_{\mathbf{q}}^{\perp}$ or α for the range of temperatures of interest, $T_{\rm g} \lesssim \phi$; further, this approximation represents a conservative estimate of the particle current, since $G(\varepsilon)$ is typically a monotonically increasing function due to the larger density of states available for scattering at larger ε in graphene.

Heat and charge currents can then be expressed in terms of non-dimensional integrals by defining $x = \varepsilon/\phi$ in Eq.(2), yielding

$$\mathcal{J}_e^{\perp} = \frac{G_0\phi}{e}\int_1^{\infty} dx\,\Delta f(x)\,,\ \mathcal{J}_{\mathbf{q}}^{\perp} = \frac{G_0\phi^2}{e^2}\int_1^{\infty} dx\,x\,\Delta f(x), \tag{4}$$

where $\Delta f(x) = f(x/\tilde{T}_{\rm g}) - f(x/\tilde{T}_0)$. It is straight-forward to show that the integrals on the right-hand side of Eq.(4) are related to the well-known complete Fermi integrals

$$F_k(\xi) = \int_0^{\infty} dx\,\frac{x^k}{e^{x-\xi}+1}, \tag{5}$$

via $\int_1^{\infty} dx x^n f(x/\tilde{T}) = \sum_{k=0}^{n}\binom{n}{k}\tilde{T}^{k+1}F_k(-1/\tilde{T})$. In the low temperature regime, $\tilde{T} \ll 1$, the value of F_k behaves as $F_k(-1/\tilde{T}) \approx \Gamma(k+1)e^{-1/\tilde{T}}$, with Γ the Gamma function. In the high temperature regime, $\tilde{T} \gg 1$, F_k takes values $F_0(-1/\tilde{T}) \approx \ln(2)$ and $F_1(-1/\tilde{T}) \approx \pi^2/12$.

Using Eq.(4) yields convective cooling $\mathcal{J}_{\mathbf{q}}^{\perp}$ that can be sizable (see blue curves in Fig. 1c). In plotting Fig. 1c, we numerically integrated Eq.(4) and used $\phi = 100\,\text{meV}$ and $G_0 = 10\,\text{mS}/\mu\text{m}^2$ (see below for G_0 estimates). Further, we find that $\mathcal{J}_{\mathbf{q}}^{\perp}$ compares favorably with electron-lattice cooling in graphene: (i) single-acoustic phonon cooling for pristine graphene $\mathcal{J}_{\mathbf{q}}^{\rm ac}$ (green curves), and (ii) disorder-assisted cooling $\mathcal{J}_{\mathbf{q}}^{\rm dis}$ (red curves), where we consider the degenerate limit ($\mu \gg T_{\rm g}$) for both cases [11–13]:

$$\mathcal{J}_{\mathbf{q}}^{\rm ac} = \gamma_{\rm ac}(T_{\rm g} - T_0), \quad \mathcal{J}_{\mathbf{q}}^{\rm dis} = \gamma_{\rm dis}(T_{\rm g}^3 - T_0^3). \tag{6}$$

Here the prefactors are $\gamma_{\rm ac} = \hbar D^2\mu^4 k_{\rm B}/8\pi\rho(\hbar v_{\rm F})^6$ and $\gamma_{\rm dis} = 2D^2\mu^2 k_{\rm B}^3/\rho c^2\hbar(\hbar v_{\rm F})^4 k_{\rm F}\ell$, with D the deformation potential, ρ the graphene mass density, and $k_{\rm F}\ell$ the dimensionless disorder parameter. In our calculations we used $\mu = \phi = 100\,\text{meV}$, $D = 20\,\text{eV}$, $\rho = 7.6\cdot10^{-7}\,\text{kg/m}^2$, and $k_{\rm F}\ell = 50$. Indeed, $\mathcal{J}_{\mathbf{q}}^{\perp}$ overwhelms $\mathcal{J}_{\mathbf{q}}^{\rm ac}$ and is competitive with $\mathcal{J}_{\mathbf{q}}^{\rm dis}$, as shown in Fig. 1c.

A key feature of hot carrier convection is the strong charge-energy current coupling $\mathcal{L}$. Using Eq.(4) above, we obtain Eq.(1) with α given by

$$\alpha(\tilde{T}_{\rm g}, \tilde{T}_0) = \frac{\int_1^{\infty} dx\Delta f(x)}{\int_1^{\infty} dx x\Delta f(x)}. \tag{7}$$

The general behavior of $\alpha(\tilde{T}_{\rm g}, \tilde{T}_0)$ can be most easily understood by first setting $T_0 = 0$. In this case, α in Eq.(1) adopts the simple form

$$\alpha_0(\tilde{T}_{\rm g}) \equiv \alpha(\tilde{T}_{\rm g}, \tilde{T}_0 = 0) = \left[1 + \tilde{T}_{\rm g}\frac{F_1(-1/\tilde{T}_{\rm g})}{F_0(-1/\tilde{T}_{\rm g})}\right]^{-1}. \tag{8}$$

Importantly, α_0 is a decreasing function of temperature $\tilde{T}_{\rm g}$, as shown in the black dashed curve of Fig. 1b. In particular, for $\tilde{T}_{\rm g} \ll 1$, α_0 takes values $\alpha_0 \sim (1+\tilde{T}_{\rm g})^{-1}$ of order unity, and for $\tilde{T}_{\rm g} \gg 1$, α_0 decreases with inverse temperature as $\alpha_0 \approx 12\log(2)/(\pi^2\tilde{T}_{\rm g})$ (see Fig. 1b). This latter fact means that, although $\mathcal{L}$ is expressed in units of e/ϕ in Eq.(1), $\mathcal{L}$ cannot grow indefinitely by making ϕ smaller; $\mathcal{L}$ reaches a saturating value $\mathcal{L} \approx 12\log(2)e/(\pi^2 k_{\rm B}T_{\rm g})$ for $T_{\rm g} \gg \phi$, as shown in Fig. 1c.

For finite values of T_0, the qualitative behavior of α does not depart significantly from that of α_0. As shown in Fig. 1b, where $\alpha(\tilde{T}_{\rm g}, \tilde{T}_0)$ is obtained by numerical integration of Eq.(7) for different values of $\tilde{T}_0$, the function α largely follows the α_0 curve and only shifts slightly from α_0 with increasing $\tilde{T}_0$. Further, the range of operating

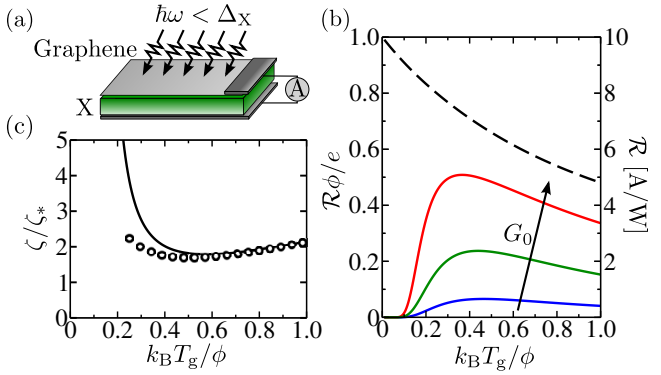

FIG. 2. (a) Schematic of a hot carrier photodetector formed by a graphene-X Schottky junction, where X is a semiconductor material with bandgap $\Delta_{\rm X}$. Here we consider graphene as the photoactive material for absorption, *i.e.* photon energy $\hbar\omega < \Delta_{\rm X}$. (b) The responsivity $\mathcal{R}$ (solid lines) for the G/X junction exhibiting a non-monotonic electronic temperature dependence peaking at $T_{\rm g} \sim \phi/2k_{\rm B}$, shown for ζ modeled in Eq.(10) [see also panel (c)] with $\zeta_* = 5, 1, 0.2$ (blue, green, red); dimensionless $\mathcal{R}$ is shown on the left vertical axis. The ζ_* values used here can be achieved e.g. using $G_0 = 2, 10, 50\,\text{mS}/\mu\text{m}^2$, with $\mu = \phi = 100\,\text{meV}$ and $k_{\rm F}\ell = 50$ yielding sizable $\mathcal{R}$ (right vertical axis). The dashed line indicates an ideal case $\mathcal{R} = \mathcal{L}$. (c) Ratio $\zeta = \mathcal{J}_{\mathbf{q}}^{\rm loss}/\mathcal{J}_{\mathbf{q}}^{\perp}$ modeled via Eq.(10) as a function of $T_{\rm g}$, with $T_0 = 0$ (solid line), and $T_0 = 300\,\text{K}$ (empty circles). Note the latter has a smaller range, $T_{\rm g} \geq T_0$.

hot electron temperatures is now smaller, $\tilde{T}_{\rm g} \geq \tilde{T}_0$, as illustrated in Fig. 1b by curves that now start at $\tilde{T}_{\rm g} = \tilde{T}_0$. Although α is finite at $\tilde{T}_{\rm g} = \tilde{T}_0$, there is no net current at equal temperatures (as indicated by the empty circles at the beginning of the curves in Fig. 1b); a non-vanishing α at $\tilde{T}_{\rm g} = \tilde{T}_0$ arises from the differential ratio that characterizes the responsivity $\mathcal{R}$.

The hot carrier convective cooling channel, $\mathcal{J}_{\mathbf{q}}^{\perp}$, and the strong charge-energy current coupling it produces [Eq.(1)], can manifest itself in large and non-monotonic responsivities in G/X photodetectors (Fig. 2a). Accounting for energy balance in Eq.(3) we find a net responsivity given by

$$\mathcal{R} = \frac{\mathcal{L}}{1+\zeta}, \quad \zeta = \frac{\mathcal{J}_{\mathbf{q}}^{\rm loss}}{\mathcal{J}_{\mathbf{q}}^{\perp}}. \tag{9}$$

To estimate ζ for actual devices, we consider the disorder-assisted cooling power in graphene [13], $\mathcal{J}_{\mathbf{q}}^{\rm loss} \approx \mathcal{J}_{\mathbf{q}}^{\rm dis} = \gamma_{\rm dis}(T_{\rm g}^3 - T_0^3)$ as an illustrative example, see Eq.(6). Adopting the same procedure as described above, we find

$$\zeta(\tilde{T}_{\rm g}, \tilde{T}_0) = \zeta_* \times \frac{\tilde{T}_{\rm g}^3 - \tilde{T}_0^3}{\int_1^\infty dx x \Delta f}\ ,\ \zeta_* = \frac{e^2\gamma_{\rm dis}\phi}{G_0}, \tag{10}$$

where the characteristic ζ is set by $e^2\gamma_{\rm dis}\phi/G_0$. As expected, increasing the prefactor $\gamma_{\rm dis}$, for $\mathcal{J}_{\mathbf{q}}^{\rm dis}$, increases the losses to phonon scattering embodied in ζ. Alternatively, increasing the conductance across the G/X interface enhances the convective cooling channel.

In calculating $\mathcal{R}$ in Eq.(9), we use the same parameter values as in Fig. 1: $\mu = \phi = 100\,\text{meV}$ and $k_{\rm F}\ell = 50$. The value of G_0 can be estimated from conductance measured in the dark state, $G_{\rm D}$, obtained in actual G/X devices at equilibrium $T_{\rm g} = T_0$ (for example G/Si Schottky junctions in Refs. [2, 3]). Indeed, under an infinitesimally small potential bias $\delta V_{\rm b}$, we can approximate Δf in Eq.(7) as $\Delta f(x) = [e^x/(e^x+1)^2] \times e\delta V_{\rm b}/T_0$ due to the small chemical potential difference $e\delta V_{\rm b}$ between G and X. Integrating over x in Eq.(7), we obtain $G_{\rm D} = G_0/(1+e^{\phi/T_0})$. In a typical scenario $T_0 \ll \phi$, the conductance in the dark state is exponentially suppressed with increasing temperature as $G_{\rm D} \approx G_0 \exp(-\phi/T_0)$, in agreement with the qualitative behavior observed in Refs. [2–8]. To give an estimate of the range of conductances achievable in G/X devices, $G_{\rm D}$ in these experiments report $G_{\rm D} \sim 0.1 - \text{several} \times \mu\text{S}/\mu\text{m}^2$ for $\phi_{\rm Si} \sim 0.3\,\text{eV}$ with T_0 at room temperature. This gives G_0 in the $G_0 \sim 1 - 100\,\text{mS}/\mu\text{m}^2$ ballpark. The responsivity $\mathcal{R}$ is plotted in Fig. 2b for three values of $G_0 = 2, 10, 50\,\text{mS}/\mu\text{m}^2$, which correspond to $\zeta_* = 5, 1, 0.2$ [see Eq.(10)].

As shown in Fig. 2c, ζ exhibits a clear non-monotonic dependence on $T_{\rm g}$ characterized by two regimes: (i) small $\tilde{T}_{\rm g} \ll 1$, $\mathcal{J}_{\mathbf{q}}^{\perp}$ is exponentially suppressed by the transport barrier ϕ, thus $\mathcal{J}_{\mathbf{q}}^{\rm dis}$ dominates, (ii) large $\tilde{T}_{\rm g} \gg 1$, we find that $\mathcal{J}_{\mathbf{q}}^{\perp}$ scales as $T_{\rm g}^2$, and rises less steeply than the $T_{\rm g}^3$ power law of supercollision cooling. Hence, there is a "sweet spot" for observing a competitive convective channel $\mathcal{J}_{\mathbf{q}}^{\perp}$. The optimal value occurs for temperatures $T_{\rm g}/\phi \approx 0.5$ (see Fig. 2c), with minimum $\zeta_{\rm min} \approx 1.85 \times \zeta_*$. This can be estimated from Eq.(10) in the limit $\tilde{T}_{\rm g} \ll 1$ and $T_0 = 0$, where the above-mentioned optimal values are obtained from minimization of the equation $\zeta/\zeta_* \approx \tilde{T}_{\rm g}^2 e^{1/\tilde{T}_{\rm g}}$ (Fig. 2c). Given that $T_{\rm g} < 2000$ K in realistic situations, Schottky barriers in the 100 meV ballpark allows operation of the G-X photodetector near optimal responsivities (i.e. near minimum ζ).

The responsivity $\mathcal{R}$ in Eq.(9) mirrors ζ to display a non-monotonic dependence on $T_{\rm g}$, peaking at a temperature $k_{\rm B}T_{\rm g} \approx 0.5\phi$, as shown in Fig. 2b. Peak responsivities in the range $\mathcal{R} \approx 1 - 10\,\text{A/W}$ are obtained within our model. Indeed, for large $G_0 = 50\,\text{mS}/\mu\text{m}^2$ (corresponding to $\zeta_* = 0.2$), $\mathcal{R}$ starts to approach the ideal case, $\mathcal{R} = \mathcal{L}$ (dashed black line). The non-monotonic dependence of $\mathcal{R}$ as a function of $T_{\rm g}$ provides a clear fingerprint of the competition between convective energy transport and conventional electron-phonon cooling. Since the Schottky barrier heights can be tuned by the applied gate voltage, the peak temperature $k_{\rm B}T_{\rm g} \approx 0.5\phi$ is gate tunable. Further, the scaling of ϕ and the device conductance G_0 also provides experimental knobs with which to adjust the responsivity of the device.

Although G/X photodetectors allow *in-situ* control of ϕ by electrostatic doping, it is important to note that several parameters of the model vary implicitly with ϕ. On the one hand, changes in ϕ also induce changes in graphene doping, thus modifying the electronic cooling power. Further, when ϕ becomes smaller than the incoming photon energies, photo-emission of primary carriers over the barrier competes with thermalization by electron-electron interactions. In this case, a smaller amount of the incident power is captured in the hot-carrier distribution.

Here we estimate the contribution of conventional diffusive modes of heat transport that can also contribute to losses $\mathcal{J}_{\mathbf{q}}^{\rm loss}$ in Eq.(3). These are the out-of-plane (vertical) and in-plane (lateral) electronic thermal conduction contributions; both of these are characterized by out-of plane (in-plane) thermal conductivity $\kappa_\perp$ ($\kappa_\parallel$). First, out-of-plane (vertical) electronic thermal conduction is exponentially suppressed by the large potential barrier. This arises because the device electrical conductance is exponentially suppressed by the large barrier $G_{\rm D} \approx G_0 \exp(-\phi/T_0)$ and is independent of $T_{\rm g}$ in this limit. As a result, a device thermal conductance for $k_{\rm B}T_0 \ll \phi$, obtained through the Wiedemann-Franz relation, is similarly suppressed. For too small ϕ, the out-of-plane electronic thermal conductance acts as a conductive channel for heat transport that competes with $\mathcal{J}_{\mathbf{q}}^{\perp}$.

Next we address lateral (in-plane) heat conduction, $\mathcal{J}_{\mathbf{q}}^{\parallel} = -\nabla \cdot (\kappa_{\parallel} \nabla T_{\rm g})$, wherein heat can be transported in sufficiently small devices to contacts that can act as heat sinks. To estimate this effect, we use the Wiedemann-Franz relation, $\kappa_{\parallel}(T_{\rm g}) = (\pi^2/3e^2) \times k_{\rm B}^2 T_{\rm g} \sigma$, where σ is the in-plane electrical conductivity of graphene. For the relevant regime of moderate to high temperatures, $T_{\rm g} \gtrsim \phi$, we can approximate $\mathcal{J}_{\mathbf{q}}^{\perp} \approx G_0 k_{\rm B}^2 T_{\rm g}^2/e^2 = \gamma^{\perp}(T_{\rm g}) \times T_{\rm g}$ [cf. Eq.(2)]. As a result, we find a cooling length $\xi_{\parallel} = \sqrt{\kappa(T_{\rm g})/\gamma^{\perp}(T_{\rm g})}$ coming from the convective channel that is independent of $T_{\rm g}$. Using a uniform in-plane $\sigma \sim 1\,\mathrm{mS}$ [23], we find $\xi_{\parallel} \approx 0.6\,\mu\mathrm{m}$, so that vertical energy extraction dominates over in-plane thermal conduction for sufficiently large devices with size $L > \xi_{\parallel}$.

Hot carrier convection described above provides new approaches for exploiting graphene optoelectronics. In particular, G/X photodetectors operated in the convective regime are markedly different from other photodetector schemes. Owing to the ultra-fast electron energy relaxation times in graphene that yield *multiple* hot carriers per absorbed photon [18, 19], G/X photodetectors can utilize the energy of photons absorbed above the Fermi energy for conversion into electrical signals. This yields enhanced $\mathcal{R}$ [Eq.(1)] for high photon frequencies, $\hbar\omega \gg \phi$ in stark contrast to PV-based schemes that yield a single electron-hole pair per absorbed photon. Further, G/X photodetectors also circumvent lateral and vertical electronic heat diffusion that reduce operating electronic temperatures in photo-thermoelectric based schemes [16]. Lastly, G/X photodetectors can also operate at low photon energies, $\hbar\omega \leq 2\mu$, where μ is the Fermi energy in graphene. In this regime, conventional Drude absorption from ambient carriers directly captures incident radiation. This contrasts with conventional semiconductor photodetectors, that do not absorb light below the semiconductor bandgap. A tantalizing possibility is to use G/X Schottky junctions within the mid IR - THz bandwidth where presently-available technologies offer lackluster performance [24, 25].

In summary, graphene Schottky junctions host tunable interfaces across which energy transport can be engineered, exemplified by a convective heat transport regime wherein energy and charge currents are strongly coupled. Fingerprints of the convective cooling regime include high responsivities on the order of $\mathcal{R} \sim 1 - 10$ A/W, and a non-monotonic dependence of $\mathcal{R}$ on electron temperature (or pump power) in G/X photodetectors. The large degree of *in-situ* tunability allows optimization of the G/X interface for different applications and irradiation conditions; vertical hot carrier convection opens up new vistas to efficiently harvest photon energies over a wide spectral range, utilizing the entire exposed graphene area as a photoactive region.

We are grateful to useful discussions with M. Baldo, M. Kats, L. Levitov. We also thank V. Fatemi, A. Frenzel, and K. Tielrooij for a critical reading. JFRN and MSD acknowledge financial support from the National Science Foundation Grant DMR1004147. JCWS acknowledges support from a Burke Fellowship at Caltech.

* jcwsong@caltech.edu

[1] A. K. Geim, I. V. Grigorieva, Nature **499**, 7459 (2013).
[2] C.-C. Chen, M. Aykol, C.-C. Chang, A. F. J. Levi, and S. B. Cronin, Nano Letters **11**, 1863 (2011).
[3] H. Yang, J. Heo, S. Park, H. J. Song, D. H. Seo, K.-E. Byun, P. Kim, I. Yoo, H.-J. Chung and K. Kim, Science **336**, 1140 (2012).
[4] L. Britnell, R. V. Gorbachev, R. Jalil, B. D. Belle, F. Schedin, A. Mishchenko, T. Georgiou, M. I. Katsnelson, L. Eaves, S. V. Morozov, *et al.*, Science **335**, 947 (2012).
[5] T. Georgiou, R. Jalil, B. D. Belle, L. Britnell, R. V. Gorbachev, S. V. Morozov, Y.-J. Kim, A. Gholinia, S. J. Haigh, O. Makarovsky, *et al.*, Nat Nano **8**, 100 (2013).
[6] X. Miao, S. Tongay, M. K. Petterson, K. Berke, A. G. Rinzler, B. R. Appleton, and A. F. Hebard, Nano Letters **12**, 2745 (2012).
[7] X. Wang, Z. Cheng, K. Xu, H. K. Tsang, and J.-B. Xu, Nat. Photonics **7**, 888 (2013).
[8] L. Britnell, R. V. Gorbachev, R. Jalil, B. D. Belle, F. Schedin, M. I. Katsnelson, L. Eaves, S. V. Morozov, A. S. Mayorov, N. M. R. Peres, *et al.*, Nano Letters **12**, 1707 (2012).
[9] W. J. Yu, Z. Li, H. Zhou, Y. Chen, Y. Wang, Y. Huang, and Xiangfeng Duan, Nat. Materials, **12**, 246 (2013)
[10] X. Li, H. Zhu, K. Wang, A. Cao, J. Wei, C. Li, Y. Jia, Z. Li, and D. Wu, Adv. Mater. **22**, 2743 (2010)
[11] R. Bistritzer, A. H. MacDonald *Phys. Rev. Lett.*, **102** 206410 (2009).
[12] W.-K. Tse, S. Das Sarma, *Phys. Rev. B*, **79**, 235406 (2009).
[13] J. C. W. Song, M. Y. Reizer, and L. S. Levitov, Phys. Rev. Lett., **109** 106602 (2012).
[14] M. W. Graham, S.-F. Shi, D. C. Ralph, J. Park, and P. L. McEuen, Nature Physics, **9**, 103 (2013).
[15] A. C. Betz, *et. al.*, Nature Physics, **9**, 109 (2013).
[16] N. M. Gabor, *et. al.*, *Science*, **334**, 648 (2011).
[17] J. Ziman, Principles of the Theory of Solids (Cambridge University Press, Cambridge, England, 1972).
[18] K.J. Tielrooij, J.C.W. Song, S.A. Jensen, A. Centeno, A. Pesquera, A. Zurutuza Elorza, M. Bonn, L.S. Levitov, and F.H.L. Koppens, Nature Physics, **9** 248 (2013).
[19] J.C.W. Song, K.J. Tielrooij, F.H.L. Koppens, and L.S. Levitov, Phys. Rev. B, **87** 155429 (2013).
[20] S. M. Sze, *The physics of semiconductor devices*, Wiley, New York (2007).
[21] J. F. Rodriguez-Nieva, M. S. Dresselhaus, and L. S. Levitov, Nano Letters **15**, 1451 (2015).
[22] J. R. Goldman, and J. A. Prybyla, Phys. Rev. Lett., **72** 1364 (1994).
[23] K. S. Novoselov, A. K. Geim, S. V. Morozov, D. Jiang, M. I. Katsnelson, I. V. Grigorieva, S. V. Dubonos and A. A. Firsov, Nature **438**, 197 (2005)
[24] W. L. Chan, J. Deibel, and D. M. Mittleman, Reports on the Progress of Physics, **70** 1325 (2007)
[25] A. Rogalski, *Infrared Detectors*, CRC Press: Boca Raton, Florida (2007).